



Filling the gap between lansfordite and nesquehonite: $\text{MgCO}_3 \cdot 4\text{H}_2\text{O}$, a new magnesium carbonate hydrate

Guntram Jordan¹ · Samuel B. Strohm¹ · Aleksandar Živković¹ · Giacomo Criniti¹ · Kai-Uwe Hess¹ · Melanie Kaliwoda^{1,2} · Elena V. Sturm¹ · Daniel Weidendorfer¹

Received: 2 October 2025 / Accepted: 31 March 2026
© The Author(s) 2026

Abstract

Formation conditions, transformation mechanisms, and transformation product selection of magnesium carbonate hydrate phases at temperatures near the freezing point of water are poorly understood. In this study, carbonated $\text{Mg}(\text{OH})_2$ suspensions were aerated at $T=0$ °C to obtain solutions from which either $\text{MgCO}_3 \cdot 6\text{H}_2\text{O}$ or lansfordite ($\text{MgCO}_3 \cdot 5\text{H}_2\text{O}$) precipitated, with the selected phase depending on the aeration rate. Subsequently, magnesium carbonate hexahydrate was subject to transformation experiments yielding five different products. The product selection depended on the transformation condition. Among the products, a new phase was identified and characterized as a neutral magnesium carbonate hydrate with the chemical composition $\text{MgCO}_3 \cdot 4\text{H}_2\text{O}$. Implications of the synthesis route and analytical results suggest that this tetrahydrate phase forms from $\text{MgCO}_3 \cdot 6\text{H}_2\text{O}$ by the release of two weakly bonded water molecules per formula unit, accompanied by a relaxation of the remaining $\text{MgCO}_3 \cdot 4\text{H}_2\text{O}$ layers without disrupting the edge-sharing octahedral pairs of the parental structure. Density functional theory calculations confirmed the stability of the proposed crystal structure through the examination of its phonon dynamics and subsequent vibrational analysis. Furthermore, the simulated X-ray powder diffraction pattern is in reasonable agreement with the experimental data when accounting for the high crystalline disorder inevitably introduced by the transformation process.

Keywords Carbonated brucite suspensions · Lansfordite · Dypingite · Hydromagnesite · Nesquehonite · Magnesium carbonate hexahydrate

Introduction

Magnesium carbonate and magnesium carbonate hydrate phases have many important implications in nature and technology. Magnesium carbonates, for instance, have been recognized as the essential phases in removal of atmospheric CO_2 via sequestration in Mg-rich host rocks or via direct air capture (e.g. Oelkers et al. 2008; McQueen et al. 2021; Yang et al. 2025). Within the $\text{MgO-CO}_2\text{-H}_2\text{O}$ system, magnesite (MgCO_3) is the most stable carbonate phase (e.g.,

Königsberger et al. 1999). Its formation, however, is kinetically hampered at Earth surface conditions (Hänchen et al. 2008; Lindner et al. 2018; Saldi et al. 2009). Phases such as hydromagnesite ($\text{Mg}_5(\text{CO}_3)_4 \cdot (\text{OH})_2 \cdot 4\text{H}_2\text{O}$) or amorphous magnesium carbonate form instead (Berninger et al. 2014; Hopkinson et al. 2012; Mavromatis et al. 2012; Shortt et al. 2024). With decreasing temperature, nesquehonite ($\text{MgCO}_3 \cdot 3\text{H}_2\text{O}$) and lansfordite ($\text{MgCO}_3 \cdot 5\text{H}_2\text{O}$) were reported to form predominantly (Ming and Franklin 1985). Below 10 °C, lansfordite was predicted to be the dominant phase (Langmuir 1965; Schott and Dandurand, 1975). However, attempts to synthesize lansfordite below 5 °C were unsuccessful in cases (Ming and Franklin 1985; Rincke 2018). Products of these attempts were nesquehonite or the recently discovered magnesium carbonate hexahydrate (Rincke et al. 2020).

Whereas the behavior and transformation reactions of nesquehonite were subject to intensive research (Davies and Bubela 1973; Harrison et al. 2019; Hopkinson et al.

✉ Guntram Jordan
jordan@lmu.de

¹ Department für Geo- & Umweltwissenschaften, Ludwig-Maximilians-Universität München, Theresienstr. 41, 80333 München, Germany

² Mineralogische Staatssammlung München, SNSB, Theresienstr. 41, 80333 München, Germany

2008; Morgan et al. 2015), little is known about magnesium carbonate hexahydrate. This situation makes it obvious that magnesium carbonate hydrate phases are insufficiently explored.

Aim of this study is to contribute to a better understanding of magnesium carbonate hydrate phases precipitating from aqueous solution close to 0 °C. As these phases are metastable in general, they are potential precursors on the routes towards the formation of more stable phases and may tremendously affect the formation rates and mechanisms of these phases.

Here, we performed experiments aiming at the formation of magnesium carbonate hexahydrate. To this end, brucite ($\text{Mg}(\text{OH})_2$) suspensions were carbonated at 0–5 °C. The subsequent aeration of the solutions resulted in a supersaturation versus various magnesium carbonate hydrate phases. Depending on the specific conditions of the syntheses, nesquehonite, lansfordite, or magnesium carbonate hexahydrate precipitated within the reactor. The obtained hexahydrate, then, was subject to transformation. Among the transformation products, a new magnesium carbonate hydrate has been identified.

Experimental

Syntheses

A four-neck glass reactor was filled with 300 g of deionized water (resistivity 18.2 M Ω cm) and equipped with a

magnetic stirring bar. The necks served as reactant feed, gas in and outlet, and as port for a standard glass pH electrode (calibrated with NIST-certified buffer solutions at the temperature of the experiment). Unused necks were kept sealed with stoppers. The reactor was placed within a low-temperature thermostat (Lauda Alpha RA 8) on top of a submerged magnetic stirrer and brought to the desired temperature. Reagent grade $\text{Mg}(\text{OH})_2$ -powder was added to the reactor (Table 1). Subsequently, the $\text{Mg}(\text{OH})_2$ -suspension was purged with CO_2 (grade ≥ 2.5 ; approx. 10 ml/sec) for up to 4 days. Upon complete dissolution of the $\text{Mg}(\text{OH})_2$ -powder, CO_2 -purging was stopped, and the reactor was subject to different re-aeration processes (Table 1). Re-aeration led to supersaturation of the solution versus magnesium carbonate hydrate phases and triggered precipitation. At various stages of the experiments, samples (up to 10 ml) were taken from the reactor. The samples were vacuum filtered. The retrieved precipitates were immediately double rinsed with pre-cooled acetone (first rinse $T=0$ °C, second rinse $T=-18$ °C) and stored at $T=-18$ °C for later analyses.

For all syntheses 300 g water was used.¹Sampling time after start of CO_2 -purging. ²MHH = magnesium carbonate hexahydrate, NSQ=nesquehonite ($\text{MgCO}_3 \cdot 3\text{H}_2\text{O}$), BRC=brucite ($\text{Mg}(\text{OH})_2$), LFD=lansfordite ($\text{MgCO}_3 \cdot 5\text{H}_2\text{O}$). ³Sampling time after start of aeration. ⁴X-ray diffractogram in SI Fig. 1. ⁵X-ray diffractogram in SI Fig. 2. ⁶X-ray diffractogram in SI Fig. 3. ⁷X-ray diffractogram in SI Fig. 4.

Table 1 Parameters and products of syntheses

Run	T [°C]	Mg(OH) ₂ [molal]	Period of CO ₂ -purging	Precipitates during CO ₂ -purging		Aeration	Precipitates triggered by aeration	
				Time ¹	Solid phase ²		Time ³	Precipitate ²
6	0	0.5	1 d	–	–	passive via orifice (Ø 2 mm)	5 d	MHH ⁴
7	0	0.5	3 d	–	–	passive via orifice (Ø 2 mm)	14 d	MHH ⁴
8	0	0.1	1 d	–	–	passive via orifice (Ø 3 mm)	3 d	MHH
							28 d	MHH ⁴
9	5	0.1	1 d	–	–	passive via orifice (Ø 2 mm)	5 d	NSQ ⁵
10	5	0.1	3 d	–	–	passive via orifice (Ø 2 mm)	2 d	NSQ ⁵
12	0	1	cont.	4 d	MHH>BRC ⁶	–	–	–
				7 d	MHH>>BRC	–	–	–
13	25	1	cont.	1 d	NSQ>>BRC ⁶	–	–	–
14	0	0.1	4 d	–	–	active with peristaltic pump (~1 mL/min)	16–42 d	MHH
							45 d	MHH>>LFD
							53 d	LFD
							67 d	LFD ⁷
15	0	0.1	2 d	–	–	active with water pump for 5 h, then passive via orifice (Ø 20 mm)	20 h	LFD
							4 d	LFD ⁷
16	0	0.1	1 d	–	–	passive via orifice (Ø 50 mm)	24 h	LFD ⁷
17	0	0.1	1 d	–	–	active via water pump for 7 h, then passive via orifice (Ø 20 mm)	3 h	LFD
							29 d	LFD ⁷

Experimental analysis of solids

X-ray powder diffraction

For phase identification, X-ray powder diffraction (XPD) was performed using a powder diffractometer (XRD3003, GE; CuK α 1 radiation) with a Ge(111) monochromator and a semiconductor position-sensitive-detector (Meteor 1D) in Bragg-Brentano geometry. XPD data was collected within a range from ≤ 10 to ≥ 50 $^{\circ}2\theta$ in 0.013 $^{\circ}$ steps. For the determination of the unknown phase, scans in the range of 5–135 $^{\circ}2\theta$ were repeated 10 times. The data were summed up for an improved signal-to-noise-ratio.

XPD phase identification and structure visualization were performed with following references:

brucite (Mg(OH) $_2$): Desgranges et al. (1996); dypingite (Mg $_5$ (CO $_3$) $_4$ ·(OH) $_2$ ·5H $_2$ O): Raade (1970); hydromagnesite (Mg $_5$ (CO $_3$) $_4$ ·(OH) $_2$ ·4H $_2$ O): Akao and Iwai (1977); lansfordite (MgCO $_3$ ·5H $_2$ O): Liu et al. (1990); nesquehonite (MgCO $_3$ ·3H $_2$ O): Giester et al. (2000); MgCO $_3$ ·6H $_2$ O: Rincke et al. (2020); Mg $_5$ (CO $_3$) $_4$ ·(OH) $_2$ ·8H $_2$ O: Suzuki and Ito (1973); shelkovite (Mg $_7$ (CO $_3$) $_5$ ·(OH) $_4$ ·24H $_2$ O): ICDD-PDF #00–047–1880 (unpublished).

ATR-Fourier-transform infrared spectroscopy

FTIR spectra were recorded on a Spectrum Two FTIR Spectrometer equipped with a monolithic diamond Gladi-ATR unit (Pike Technologies) and the software Spectrum 10 (PerkinElmer). The samples were measured without further sample preparation by applying the powder directly onto the diamond of the ATR unit. The spectra were recorded within the range of 400–4000 cm^{-1} and a spectral resolution of 4 cm^{-1} . In the raw spectra, baseline and atmospheric interferences were corrected. The presented data were averaged over a total of 100 scans.

Raman spectroscopy

Raman spectra were taken with a HORIBA Jobin Yvon XploRa ONE confocal Raman microscope equipped with Olympus LMPlanFL N lenses, an 1800 T grating, and a 2 ω -Nd: YAG laser ($\lambda = 532$ nm) with an undimmed intensity resulting in a laser power of 8 mW on the sample surface for the 50x large working distance lens used here. Slit and hole dimensions were set to 200 μm and 300 μm , respectively. Calibration was performed using a silicon reference sample with a dominant band at 520 ± 1 cm^{-1} . The device maintains an overall Raman shift accuracy of ± 1.5 cm^{-1} . Spectra were recorded in the range 50–4000 cm^{-1} in triplicate (total data acquisition time 3 \times 120 s).

Thermogravimetric analysis

Thermogravimetric analysis (TGA) was carried out using a Netzsch STA 449 F1 thermal analyzer. A sample of the new unknown phase with a mass of 8.28 mg was placed in an uncovered Al $_2$ O $_3$ crucible and heated to 400 $^{\circ}\text{C}$ in static air atmosphere (ramp rate 2 K/min).

Combustion elemental analysis

Hydrogen and carbon contents of the new unknown phase were analyzed with a ThermoScientificTM FlashSmartTM elemental analyzer operating with a modified Dumas method. 2.5–6.4 mg of sample material were placed in tin containers and combusted with high-purity oxygen. Helium acted as carrier gas for the transport to an adjacent gas chromatograph, in which hydrogen was detected by thermal conductivity. The elemental analyzer was calibrated using a BBO^T standard and checked with secondary standards before and after the measurement of three replicates of the sample.

Scanning electron microscopy

For an evaluation of the morphology of the crystals and for the investigation of potential pseudomorphic relations, images were taken with a scanning electron microscope (SEM; Hitachi SU 5000) operating under an accelerating voltage of 20 kV.

Computational details

First principles

Density functional theory (DFT) calculations were performed using the all-electron (AE) code CRYSTAL (Dovesi et al. 2018; Erba et al. 2023; Pascale et al. 2004; Zicovich-Wilson et al. 2004). Unless stated otherwise, the global hybrid B3LYP exchange-correlation functional was used (Becke 1993; Lee et al. 1988) together with the Peintinger-Oliveira-Bredow triple- ζ -valence+ polarization basis set (pob-TZVP rev2, Vilela Oliveira et al. 2019). The mixing of non-local Fock and semi-local exchange provides a reliable representation of electronic and structural properties of a range of oxide compounds (Harrison 2001; Muscat et al. 2001; Patel et al. 2012). The Coulomb and exchange series are summed directly and truncated using overlap criteria with thresholds of 10^{-7} , 10^{-7} , 10^{-7} , 10^{-7} , and 10^{-14} , as described previously (Dovesi et al. 2017; Pisani et al. 1988). Reciprocal space (Monkhorst and Pack 1976) was sampled according to a shrinking factor (input IS) of (5 9 5) for nesquehonite, (8 8 4) for lansfordite, (5 5 5) for hydromagnesite, and (5 7 5) for hexahydrate. Long range

dispersion corrections were included using the semiempirical D3 approach of Grimme et al. (2010, 2011, 2016) with Becke-Johnson damping.

Ab-initio molecular dynamics (AIMD)

AIMD simulations were conducted using the Vienna ab-initio simulation package (VASP) with the projector augmented-wave (PAW) method (Kresse and Furthmüller 1996a, b; Kresse and Joubert 1999). For the PAW potentials, the valence electronic configurations used were $3s^2$ for Mg, $2s^2sp^2$ for C, s^2p^4 for O and s^1 for H. An energy cutoff of 480 eV was used to truncate the plane-wave expansion. The general gradient approximation (GGA) for the exchange-correlation (XC) functional was employed within the Perdew-Burke-Ernzerhof parametrization (PBE, Perdew et al. 1996), where long-range dispersion corrections were included using the D3 approach of Grimme (2006).

AIMD runs were performed with a time-step of 0.5 fs. We used a $1 \times 2 \times 2$ supercell of the dehydrated hexahydrate structure optimized earlier in the isobaric-isothermal NpT ensemble (Langevin thermostat) with the Brillouin zone integrated with a $2 \times 2 \times 2$ k-mesh. An initial thermalization of at least 2.5 ps was performed before a sampling period of at least 2.5 ps was undertaken. To mimic the experimentally observed conditions closely, the thermostat temperature and pressure were set to 300 K and 1 atm, respectively.

Machine learning

On top of the obtained AIMD datasets, machine learning interatomic potentials were trained using the MLIP package (v2, Novikov et al. 2021), which allows for moment tensor potentials (MTPs) to be constructed. Since the AIMD trajectories are correlated within short time periods, only every 10th step of the original trajectories was included in the respective initial training set. Next, MTPs of different levels (18 and 20) were parameterized to describe the interatomic interactions. For computational efficiency, MTPs were first trained over subsampled AIMD trajectories. After the preliminary training of MTPs, the accuracy of the trained potentials was evaluated over the full AIMD trajectories and the configurations with high extrapolations grades are identified (Podryabinkin and Shapeev 2017). Such selected configurations were then added to the original training sets and the final MTPs were developed by retraining clean potentials over the updated training sets. We have used the default weights that express the importance of energies and forces and stresses in optimizing MTPs, i.e., they were set to 1, 0.1, and 0.001, respectively. The MLIP_PHONOPY code was used to assess the phonon spectra directly from the trained MTPs (Mortazavi et al. 2020). Phonon band

structure calculations were performed on optimized DFT geometries along high-symmetry directions obtained using the SeeK-path interface (Hinuma et al. 2017).

Results & discussion

Products of syntheses

The synthesis experiments (Table 1) can be divided into four groups.

Group 1: Syntheses with a slow aeration rate via a diffusive exchange of CO_2 for air through a small orifice ($\varnothing=2-3$ mm) or via slow pumping of air at $T=0$ °C (experiments #6-#8 and #14).

Group 2: Syntheses with a slow aeration rate at $T=5$ °C (experiments #9 and #10).

Group 3: Syntheses with high magnesium concentrations at $T=0$ and 25 °C (experiment #12 and #13).

Group 4: Syntheses with either rapid initial active aeration or passive aeration with a large-diameter orifice at $T=0$ °C (experiments #15-#17).

The comparison of the products of the synthesis groups 1 and 4 ($T=0$ °C) shows that the aeration rate was the crucial parameter for the formation of magnesium carbonate hexahydrate on the one hand and lansfordite on the other hand. Slow aeration (synthesis group 1) caused a slow increase of the pH-value of the solution and, therefore, a slow increase of the CO_3^{2-} concentration of the solution. Formation of magnesium carbonate hexahydrate was the consequence. Fast aeration (synthesis group 4) not only caused a more rapid increase of the pH-value and, thus, of the CO_3^{2-} concentration but also led to a higher pH_{max} -value at the moment of the onset of precipitation.

Although the pH_{max} -values at the start of product phase precipitation could not be determined systematically, values were obtained in a few experiments and allowed for a qualitative assessment of precipitation conditions. In experiment #15, the pH_{max} -value in the moment of lansfordite precipitation was approx. 9.1. In experiment #8, a pH_{max} -value of approx. 8.6 was reached in the moment of magnesium carbonate hexahydrate precipitation. Lansfordite precipitation, thus, required a higher CO_3^{2-} concentration in solution than magnesium carbonate hexahydrate.

Attempts to increase solution supersaturation by increasing the magnesium concentration via adding more brucite (synthesis group 3) did not yield lansfordite. In these experiments, the product phase had started precipitating before all brucite was dissolved by CO_2 purging.

Syntheses at $T=5$ °C and 25 °C yielded nesquehonite irrespectively of the amount of brucite reactant (cf. experiments #9, #10, and #13). The precipitation of nesquehonite

Table 2 Transformation of magnesium carbonate hexahydrate

Type #	Environment	Temperature [°C]	Transformation product	Remarks
i	mother liquor	0	lansfordite	onset of transformation not detected before 45 days (exp. #14)
ii	closed container	20	basic magnesium carbonate hydrate (dypingite-like)	XRD shows no satisfying match with known reference patterns
iiib	open container (ambient air)	50	hydromagnesite	Transformation rate depends strongly on temperature
iiia		20–50	new magnesium carbonate hydrate: $\text{MgCO}_3 \cdot 4\text{H}_2\text{O}$	
iiib		120	amorphous phase	

at 5 °C in our experiments corroborates the findings of Ming and Franklin (1985) and Rinke (2018) who reported nesquehonite precipitation at a temperature of even 4 °C and 0 °C, respectively.

After the onset of magnesium carbonate hexahydrate precipitation (experiments #6–#8, #14), the reactivity of the system became low. For up to 42 days, magnesium carbonate hexahydrate was the only phase in samples which were retrieved from the reactor, filtered, and analyzed by XPD (experiment #14; see Table 1). In the sample retrieved 3 days later (total aeration time: 45 days), lansfordite was detected besides magnesium carbonate hexahydrate. Another 8 days later (total aeration time: 53 days), magnesium carbonate hexahydrate was no longer detectable. This transformation indicated that lansfordite is more stable

than magnesium carbonate hexahydrate. Lansfordite did not undergo any transformation in mother liquor within the time frame of observation (29 days; experiment #17). Possible transformation of nesquehonite in mother liquor was not in the focus of this study.

Transformation products of magnesium carbonate hexahydrate

The magnesium carbonate hexahydrate crystals synthesized in experiments #6–#8 and #14 (Table 1) transformed into different products in different environments (Table 2).

Transformation type i) As described above, magnesium carbonate hexahydrate in mother liquor at $T=0$ °C transformed into lansfordite after 45 days (experiment #14).

Transformation type ii) Magnesium carbonate hexahydrate placed within a closed container at $T=20$ °C for 21 days (approx. 1 g within a 40 ml polypropylene container) transformed into a basic magnesium carbonate hydrate phase. The X-ray diffractogram matches with known phases very poorly (Fig. 1). A weak correlation exists with the data for dypingite ($\text{Mg}_5(\text{CO}_3)_4 \cdot (\text{OH})_2 \cdot 5\text{H}_2\text{O}$, Raade 1970) and $\text{Mg}_5(\text{CO}_3)_4 \cdot (\text{OH})_2 \cdot 8\text{H}_2\text{O}$ (Suzuki and Ito 1973). The ATR-FTIR spectrum (Fig. 2) of the material reveals two prominent sharp CO_3^{2-} stretching bands at 1424 and 1481 cm^{-1} and a band at 3649 cm^{-1} . The latter is an indication of an almost free OH^- vibration (White 1971) and supports the assumption of a dypingite-like basic magnesium carbonate hydrate. For dypingite and dypingite-like phases, Lu et al. (2025) recently pointed out a correlation between the shift of the XPD-peak at 8.33 ° 2θ (Cu $K\alpha$) towards higher diffraction angles on the one hand and the water content of the crystal on the other hand. The respective XPD-peak of our phase lies at ~ 7.7 ° 2θ (Cu $K\alpha$) and, therefore, might indicate the presence of even more than eight molecules

Fig. 1 X-ray powder diffractogram (CuK α 1 radiation) of the transformation product of $\text{MgCO}_3 \cdot 6\text{H}_2\text{O}$ in air within a closed container at 20 °C after 21 days (transformation type *ii*_a; black, top), and diffractograms of dypingite (Raade 1970; red, second from top), $\text{Mg}_5(\text{CO}_3)_4 \cdot (\text{OH})_2 \cdot 8\text{H}_2\text{O}$ (Suzuki and Ito 1973; green, third from top), $\text{MgCO}_3 \cdot 6\text{H}_2\text{O}$ (Rincke et al. 2020; blue, bottom)

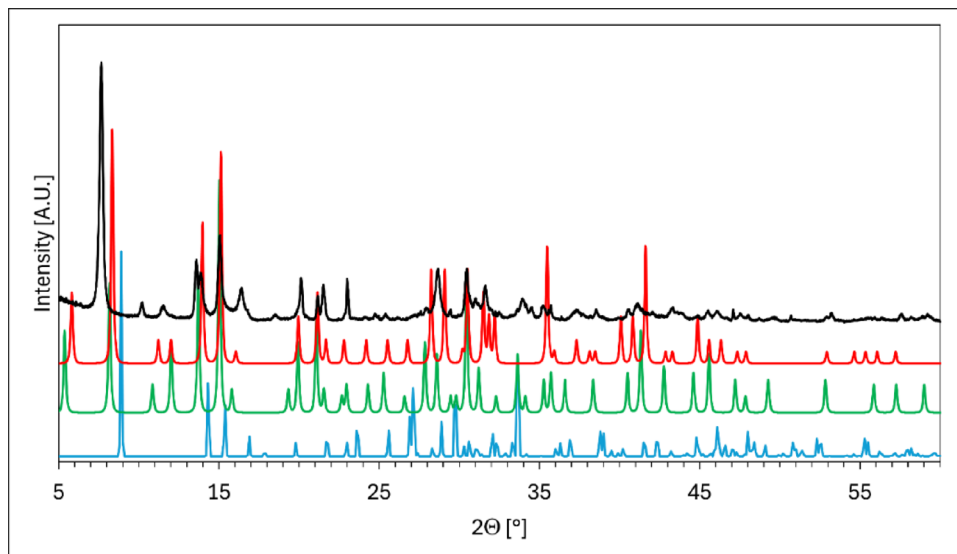


Fig. 2 FTIR-spectrum of the transformation product of $\text{MgCO}_3 \cdot 6\text{H}_2\text{O}$ in air within a closed container at 20°C after 21 days (transformation type *iii*)

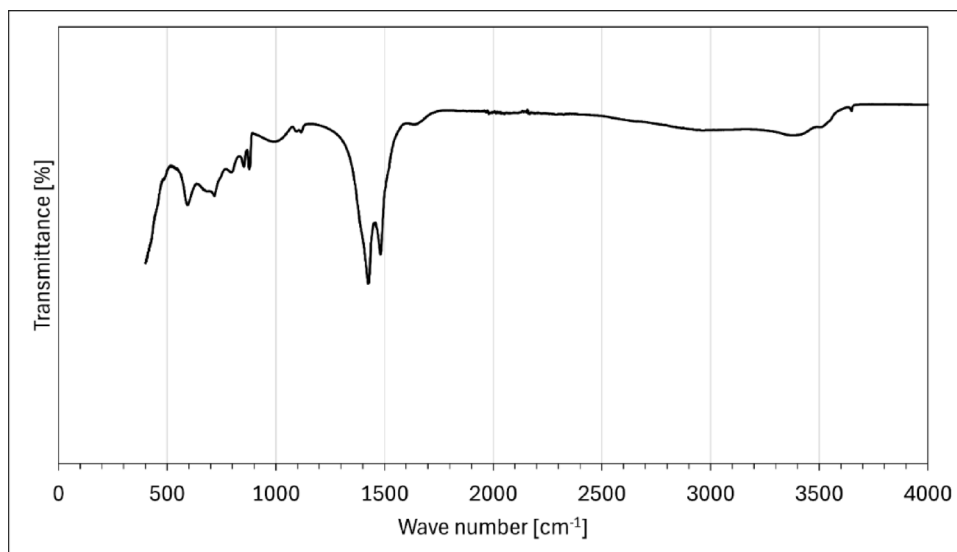
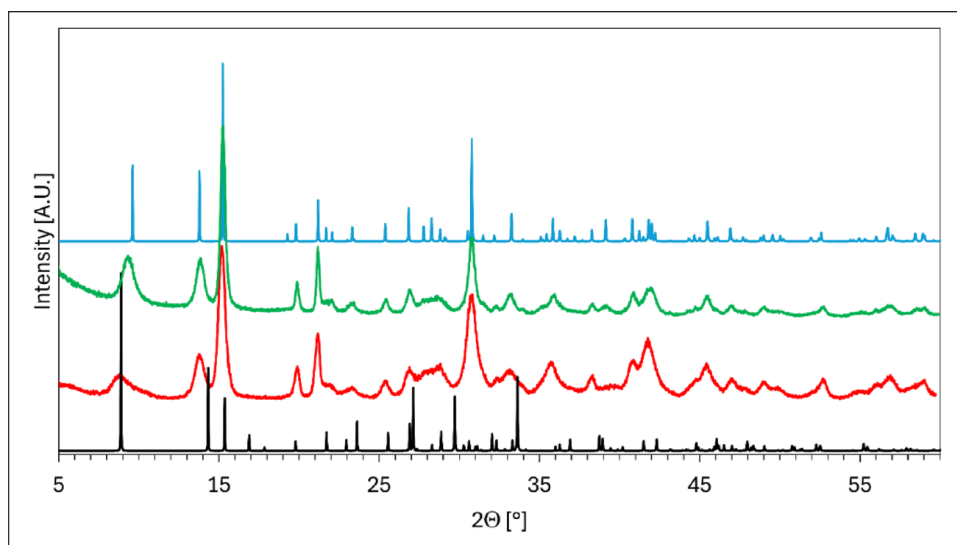


Fig. 3 Comparison of the X-ray powder diffractograms (CuK α 1 radiation) of $\text{MgCO}_3 \cdot 6\text{H}_2\text{O}$ (Rincke et al. 2020; black, bottom), its transformation product in air within a closed container at 50°C (transformation type *iib*) after 9 days (red, second from bottom), after 4 months (green, third from bottom), and the diffractogram of hydromagnesite (Akao and Iwai 1977; blue, top)



of water per formula unit for the transformation product of magnesium carbonate hexahydrate in a closed container at $T=20^\circ\text{C}$.

Transformation type iib) After 9 days within a closed container at $T=50^\circ\text{C}$ (approx. 1 g within a 40 ml polypropylene container), the transformation product revealed an XPD pattern which reasonably matched the pattern of hydromagnesite (Fig. 3). Within the next 4 months, the pattern of the transformation product did undergo only little changes.

The FTIR-spectrum of the product reveals CO_3^{2-} stretching bands at 1418 cm^{-1} and 1481 cm^{-1} as well as a OH^- stretching band at 3649 cm^{-1} (Fig. 4). This spectrum is in accordance with published data for hydromagnesite (White 1971: 1420 cm^{-1} , 1475 cm^{-1} , and 3658 cm^{-1} ; Raade 1970: 1420 cm^{-1} , 1480 cm^{-1} , and 3650 cm^{-1}). Furthermore, the spectrum is very similar to the spectrum of the

transformation product obtained at $T=20^\circ\text{C}$ (Fig. 2). Based on this similarity, Raade (1970) suggested a close structural relationship between the two basic magnesium carbonate hydrate minerals hydromagnesite and dypingite.

Transformation type iiii) Transformation of magnesium carbonate hexahydrate openly exposed to air between room temperature and $T=50^\circ\text{C}$ yielded a new magnesium carbonate hydrate. The transformation rate depended on temperature. At $T=50^\circ\text{C}$, completion of the transformation took few hours. At $T=20^\circ\text{C}$, XPD indicated about 9%, 3%, 2% magnesium carbonate hexahydrate remaining after one, three, six weeks, respectively (SI Fig. 5). The new magnesium carbonate hydrate is characterized below.

Transformation type iiib) Transformation product of magnesium carbonate hexahydrate openly exposed to air at $T=120^\circ\text{C}$ was an amorphous phase (SI Fig. 6). The formation of an amorphous phase from crystalline magnesium

Fig. 4 FTIR-spectrum of the transformation product of $\text{MgCO}_3 \cdot 6\text{H}_2\text{O}$ in air within a closed container at 50 °C after 4 months (transformation type *iib*)

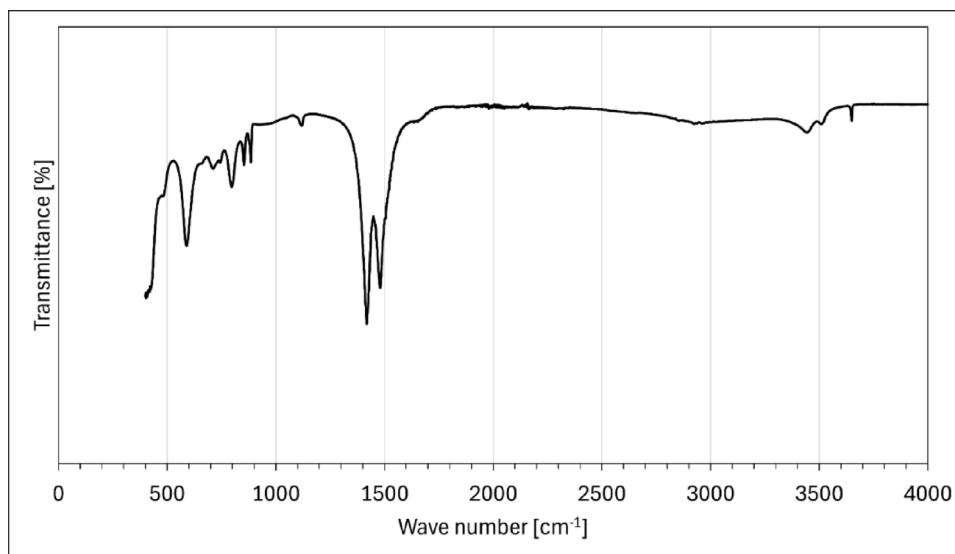
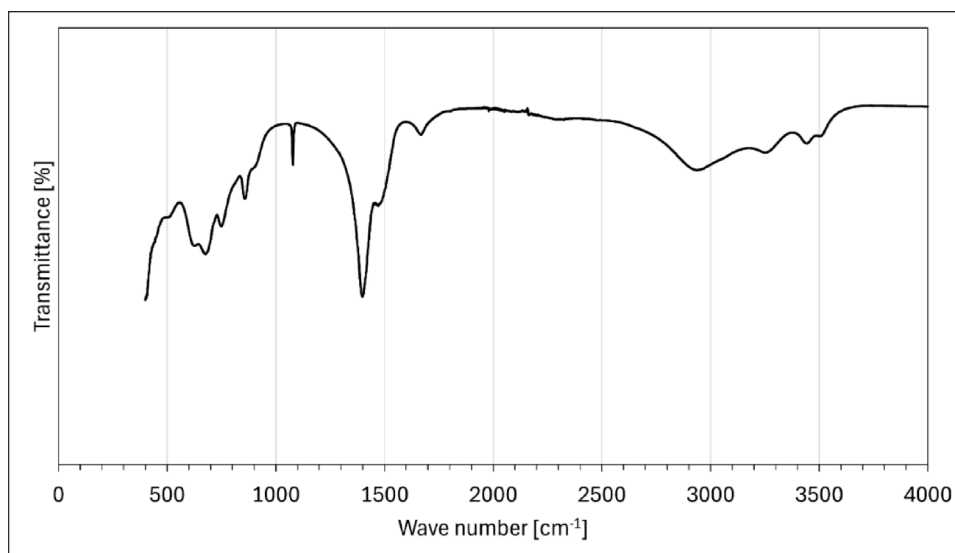


Fig. 5 FTIR spectrum of the new magnesium carbonate hydrate phase (transformation type *iiia*)



carbonate hydrate phases at elevated temperatures has been reported previously in various contexts (Dell and Weller 1959; Lanas and Alvarez 2004; Morgan et al. 2025).

Transformation within a closed small container (transformation type *ii*) led to different products than if the crystals were openly exposed to ambient air (transformation type *iii*). In the closed system, initial dehydration of magnesium carbonate hexahydrate led to increasing moisture within the container. This moisture may enable transport of constituents and a substantial structural re-organization of the magnesium carbonate hexahydrate building units (i.e., the $\text{Mg}_2(\text{CO}_3)_2(\text{H}_2\text{O})_8$ units), which led to a dypingite-like phase ($T=20$ °C) or to hydromagnesite ($T=50$ °C). If openly exposed to ambient air (transformation type *iii*), magnesium carbonate hexahydrate transformed into an amorphous phase ($T=120$ °C) or into a new magnesium carbonate hydrate ($T=20$ – 50 °C).

Experimental characterization of the new magnesium carbonate hydrate (transformation type *iiia*)

ATR-Fourier-transform infrared spectroscopy

The FTIR spectrum (Fig. 5) of the transformation product of $\text{MgCO}_3 \cdot 6\text{H}_2\text{O}$ exposed to ambient air in open containers (transformation type *iiia*) revealed no sharp band at approx. 3650 cm^{-1} . Such a band would be observed if (almost) free hydroxyl groups were present in the structure (cf. Botha and Strydom 2003; Raade 1970; White 1971). The FTIR analysis, therefore, indicated that the new phase is not a basic magnesium carbonate hydrate.

Fig. 6 Raman spectrum of the new magnesium carbonate hydrate (black, top). The marked Raman bands are located at 129, 185, 250, 409, 708, 871, 914, 1085, 1421, 1654, 1738, 2332, 3071, 3273, 3431, 3500 cm^{-1} . For comparison, a spectrum of nesquehonite retrieved from synthesis run #10 (cf. Table 1) was inserted (red, bottom)

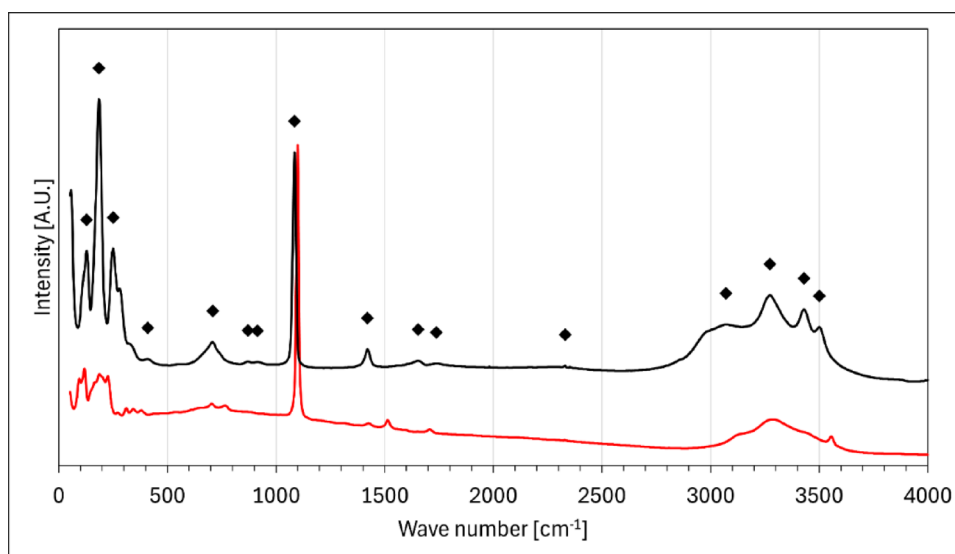


Table 3 Percentages of elemental carbon and hydrogen of magnesium carbonate hydrate phases as compiled by Canterford et al. (1984) along with further selected compositions (ordered by increasing carbon weight%)

Phase	Number of components			Molar weight	Carbon [wt%]	Hydrogen [wt%]
	MgCO ₃	Mg(OH) ₂	H ₂ O			
artinite	1	1	3	196.677	6.11	4.10
shelkovite ¹	5	2	24	970.563	6.19	5.40
MgCO ₃ ·6H ₂ O	1	0	6	192.403	6.24	6.29
lansfordite	1	0	5	174.388	6.89	5.78
MgCO ₃ ·4H ₂ O	1	0	4	156.373	7.68	5.16
new phase (exp. values)					7.75	5.23
protohydromagnesite ¹	4	1	11	593.736	8.09	4.07
pokrovskite	1	1	0	142.632	8.42	1.41
nesquehonite	1	0	3	138.358	8.68	4.37
Mg ₅ (CO ₃) ₄ ·(OH) ₂ ·8H ₂ O	4	1	8	539.691	8.90	3.36
giogiosite	4	1	6	503.661	9.54	2.80
dypingite	4	1	5	485.646	9.89	2.49
barringtonite ¹	1	0	2	120.343	9.98	3.35
hydromagnesite	4	1	4	467.631	10.27	2.16

¹As of January 2026, this phase is not approved as a mineral by the International Mineralogical Association IMA

Raman spectroscopy

The Raman spectrum of the new phase corroborated the interpretation of the FTIR spectrum (Fig. 6): no Raman shift occurred above 3500 cm^{-1} . The new phase, therefore, is not a basic but a neutral magnesium carbonate hydrate. Raman bands of the new phase were located at 129, 185, 250, 409, 708, 871, 914, 1085, 1421, 1654, 1738, 2332, 3071, 3273, 3431, 3500 cm^{-1} . For comparison, the Raman spectrum of nesquehonite (product of experiment #10) was inserted in Fig. 6. Although the strongest bands of nesquehonite (1099 cm^{-1} , symmetric CO₃²⁻ stretching) and the new magnesium carbonate hydrate (1085 cm^{-1}) were close, the two spectra were clearly resulting from two different phases. Based on the symmetric CO₃²⁻ stretching band,

Rinke et al. (2020) speculated that magnesium carbonate hexahydrate transforms into nesquehonite. For the conditions tested here, such a transformation can be discarded.

Combustion elemental analysis

The percentages of elemental carbon and hydrogen of the new magnesium carbonate hydrate were (7.75 ± 0.02) % and (5.23 ± 0.01) %, respectively. Table 3 gives a compilation of the carbon and hydrogen percentages of various basic and neutral magnesium carbonate hydrates (ordered by increasing carbon weight%). The two phases with the closest carbon concentrations are Mg₅(CO₃)₄·(OH)₂·11H₂O (protohydromagnesite) and MgCO₃·4H₂O. Protohydromagnesite, however, has a much lower hydrogen concentration and is

Fig. 7 Thermogravimetric analysis of the new magnesium carbonate hydrate. From top to bottom, the four horizontal lines give the theoretical weight% of completely dehydrated $\text{MgCO}_3 \cdot 3\text{H}_2\text{O}$ (nesquehonite), $\text{MgCO}_3 \cdot 4\text{H}_2\text{O}$, $\text{MgCO}_3 \cdot 5\text{H}_2\text{O}$ (lansfordite), and $\text{MgCO}_3 \cdot 6\text{H}_2\text{O}$

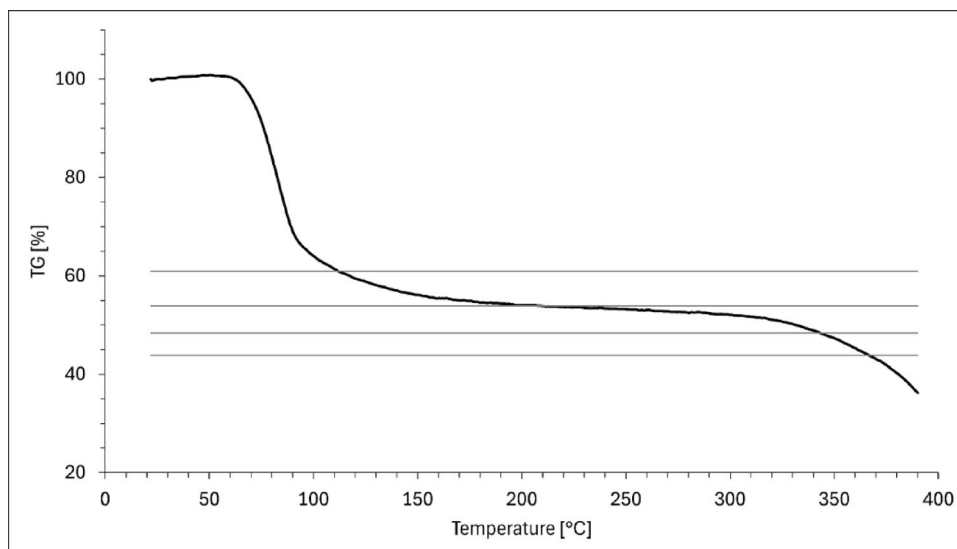
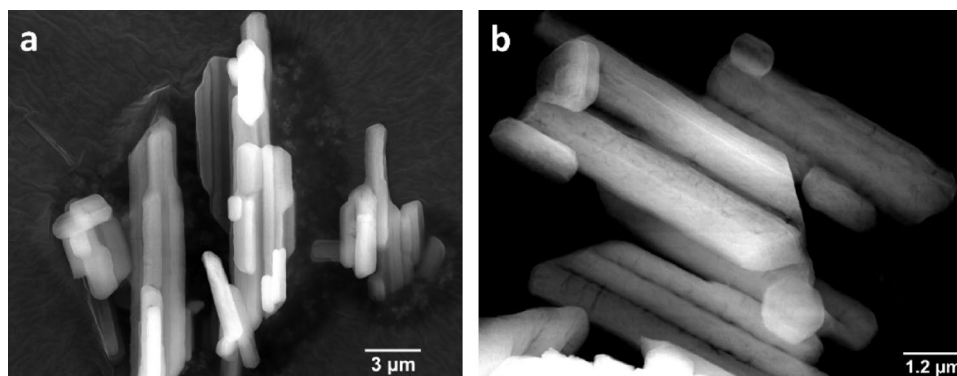


Fig. 8 SEM micrographs (secondary electrons, acceleration voltage 20 kV) of the new magnesium carbonate hydrate phase reveal acicular crystals which partially form prismatic aggregates



a basic magnesium carbonate hydrate. As FTIR and Raman spectroscopy did not indicate the presence of hydroxyl groups, protohydromagnesite can be discarded as possible match for the new phase. Magnesium carbonate tetrahydrate fits best to the result of combustion elemental analysis.

Thermogravimetric analysis

Thermogravimetric analysis of the new magnesium carbonate hydrate revealed a two-step decomposition process (Fig. 7). A first mass loss was observed between room temperature and approx. 250 °C. A second followed above 250 °C. The first mass loss can be assigned to the release of water. Quantitative evaluation of the data gave a mass loss of 47 ± 2 wt% which corresponds to a theoretical formula of $\text{MgCO}_3 \cdot (4.2 \pm 0.4)\text{H}_2\text{O}$. The data, therefore, fits best to a phase with a composition of $\text{MgCO}_3 \cdot 4\text{H}_2\text{O}$.

Scanning electron microscopy

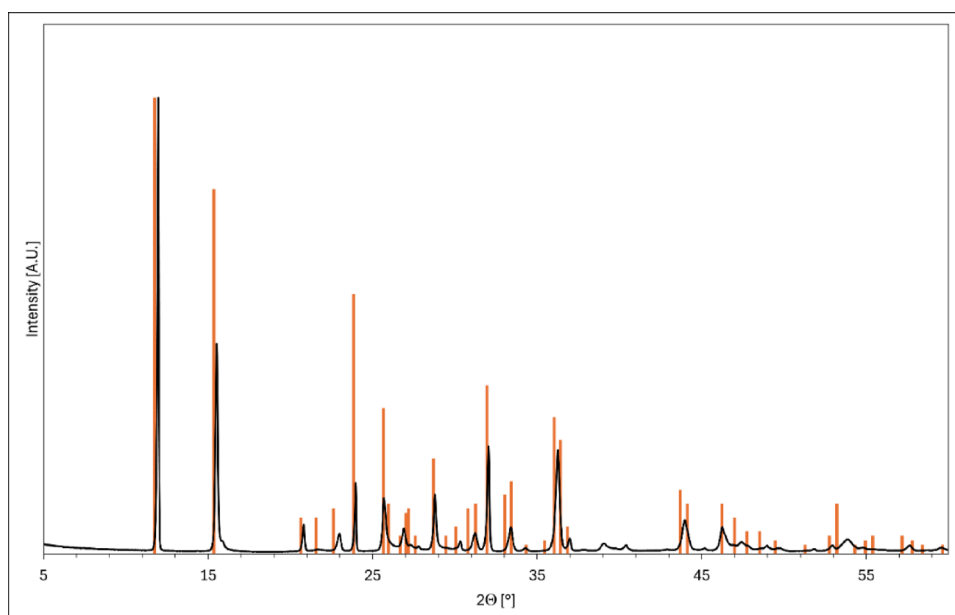
SEM imaging (Fig. 8) showed an acicular crystal habit of the new phase. Individual needles reached diameters of up to

about 1 μm and lengths of few tens of micrometers. Besides individually located needles, prismatic aggregates of parallelly oriented needles were found frequently. The prismatic habit of these aggregates may be initiated by a pseudomorphism after magnesium carbonate hexahydrate. The finding is corroborated by Rincke et al. (2020) who reported prismatic crystals of magnesium carbonate hexahydrate and an acicular habit for the transformation product. As the transformation essentially comprises dehydration within a dry environment, transport of constituents is unlikely part of the transformation mechanism. Structural collapse rather than substantial re-organization of structural constituents, therefore, may dominate the transformation.

X-ray powder diffraction

The XPD pattern of the new magnesium carbonate hydrate (Fig. 9) was compared with literature data. Closest match was observed with PDF #00–047–1880 (Vasilev & Chesnokov, private communication, 1995) of the International Centre for Diffraction Data (ICDD). PDF #00–047–1880 lists d -values and lattice parameters ($a = 6.758$ Å, $b = 15.019$ Å,

Fig. 9 X-ray powder diffractogram (CuK α radiation) of the new magnesium carbonate hydrate (black) with the XPD pattern generated from the data of ICDD-PDF #00–047–1880 (unpublished, red)



$c=10.003 \text{ \AA}$; $\beta=121.080^\circ$) for a monoclinic phase called “shelkovite” without reporting any space group and proposes a chemical composition of $\text{Mg}_7(\text{CO}_3)_5 \cdot (\text{OH})_4 \cdot 24\text{H}_2\text{O}$. For illustrative purposes, the PDF-data and our experimental data can be superimposed (Fig. 9). The comparison reveals that the peak list positions of shelkovite does not include all peak positions observed here, and that peak positions are shifted in 2θ . Our combustion elemental analysis (Table 3) and thermogravimetric analysis (Fig. 7), moreover, preclude a composition of $\text{Mg}_7(\text{CO}_3)_5 \cdot (\text{OH})_4 \cdot 24\text{H}_2\text{O}$ for the new phase. Our FTIR and Raman spectroscopy analyses (Figs. 5 and 6), furthermore, confirm the absence of hydroxyl groups and imply that the new phase is not a basic magnesium carbonate hydrate.

Recently, Santamaría-Pérez et al. (2024) reported a series of XPD peaks which they could not allocate to a known phase. Based on these XPD peaks, the authors concluded a potential formation of $\text{MgCO}_3 \cdot 4\text{H}_2\text{O}$ at 0.7 GPa and 115 °C (orthorhombic lattice; $a=9.183 \text{ \AA}$, $b=5.736 \text{ \AA}$, $c=5.324 \text{ \AA}$). A conversion of their first four strong peaks to 2θ positions with Cu $K_{\alpha 1}$ radiation gives 18.3°, 19.4°, 24.8°, and 30.1°. A comparison with Fig. 9 shows that none of their peaks matches ours. As Santamaría-Pérez et al. (2024) did not provide any further chemical or structural analysis, the identity of their phase remains unclear.

Numerical characterization of the new magnesium carbonate hydrate

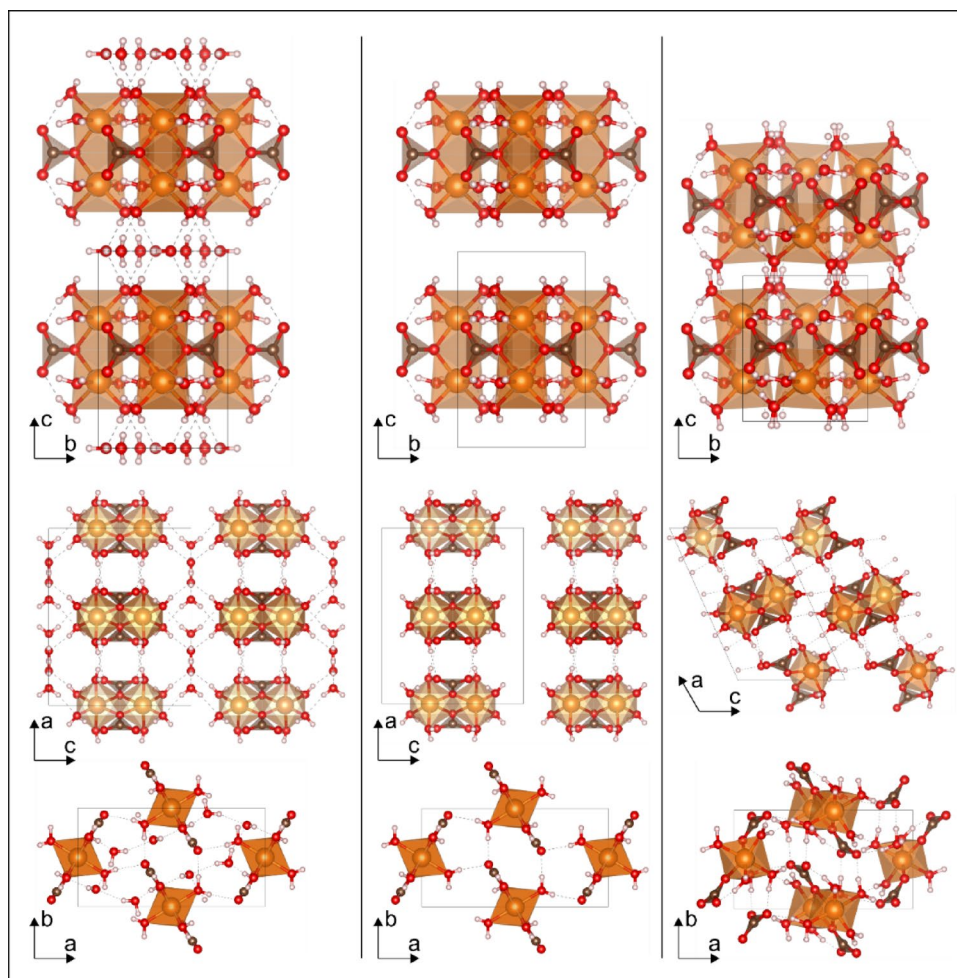
Our analyses revealed that the transformation type *iiia* corresponds to a dehydration of magnesium carbonate hexahydrate by two water molecules per formula unit yielding magnesium carbonate tetrahydrate. In the structure of

magnesium carbonate hexahydrate, four of the six water molecules coordinate Mg^{2+} ions and two water molecules are integrated within the structure only by hydrogen bonds. These two water molecules form layers in between magnesium carbonate tetrahydrate layers (Fig. 10) and are very likely more easily released than the water molecules coordinating Mg^{2+} ions (four per formula unit). Consequently, we propose that the transformation from hexahydrate to tetrahydrate takes place via the release of the two water molecules located between the magnesium carbonate tetrahydrate layers. A structural re-organization of the building units of the parental hexahydrate phase, therefore, is not required to attain the chemical composition of the product phase. The release of the two water molecules (per formula unit) along with a structural collapse of the remaining magnesium carbonate tetrahydrate layers is sufficient to accomplish the transformation. Scanning electron microscopy (Fig. 8) showed that the new magnesium carbonate hydrate frequently forms prismatic aggregates of parallel needles. These prismatic aggregates indicate a pseudomorphism after hexahydrate (cf. Rincke et al. 2020) and support the idea of a structural collapse of the partially dehydrated magnesium carbonate hexahydrate.

Structure of $\text{MgCO}_3 \cdot 4\text{H}_2\text{O}$ calculated using DFT

First-principles simulations require information about the lattice parameters, the atomic species and coordinates. Because there is a lack of such information from either the literature or the outlined measurements, we started from the parental hexahydrate structure, removed the free-standing water molecules located between the magnesium carbonate tetrahydrate layers, and relaxed the structure into its ground

Fig. 10 Crystal structure of magnesium carbonate hexahydrate ($\text{MgCO}_3 \cdot 6\text{H}_2\text{O}$, Rincke et al. 2020; left column), the structure of $\text{MgCO}_3 \cdot 6\text{H}_2\text{O}$ upon removal of the two free water molecules (central column), and the structure of $\text{MgCO}_3 \cdot 4\text{H}_2\text{O}$ (right column) after relaxation calculated using DFT. The Figure has been generated with VESTA (Momma and Izumi 2011). Colour coding of the spheres: magnesium=orange, oxygen=red, carbon=black, hydrogen=white



state without any additional constraints on the lattice or atomic positions (Fig. 10).

Upon the removal of the free-standing interlayer water, the structure collapsed along the z-axis due to the lack of repulsion between the remaining magnesium carbonate tetrahydrate layers, and further underwent a tilting of the octahedra with respect to each other to form a closer packed structure compared to the parental hexahydrate (Fig. 10). Important to note, none of the edge-sharing octahedral pairs of the hexahydrate structure (i.e., the $\text{Mg}_2(\text{CO}_3)_2(\text{H}_2\text{O})_8$ units) had undergone any decomposition or transition e.g. into corner-sharing octahedral pairs. Computing more advanced properties such as the energetics of hydration in the $\text{MgO}-\text{CO}_2-\text{H}_2\text{O}$ system would be an interesting prospect for future work but would likely require a more careful approach (e.g., Chaka and Felmy 2014).

Phonon dispersion of the calculated $\text{MgCO}_3 \cdot 4\text{H}_2\text{O}$ structure

When studying any new structure, it is crucial to examine its lattice dynamics and atomic vibrations to confirm the dynamic stability of the proposed system. Without doing so,

one risks predicting materials which turn out to be unstable and impossible to synthesize (Zunger 2019). The stability of a crystal lattice depends on three fundamental conditions (Lukačević 2011):

- i No net forces on atoms: Each atom must be in mechanical equilibrium, meaning the total force acting on it is zero.
- ii Resistance to large-scale distortions: The lattice must remain stable under macroscopic deformations.
- iii The crystal remains stable against small displacements. For any displacement of atoms, there is a restoring force that brings them back to equilibrium.

The latter can be reformulated in terms of vibrations of the lattice (phonons): all phonon frequencies must be positive. Negative (imaginary) frequencies would indicate that the lattice is unstable and would spontaneously distort into a new arrangement. The last condition, therefore, is directly connected to the soft-mode theory of structural phase transitions. According to this theory, when an external parameter such as temperature, pressure, or an applied electric or

magnetic field is varied, the frequency of a particular vibrational mode can gradually decrease (“soften”). When the frequency approaches zero, the restoring force disappears, signaling that the lattice has become unstable. The system then undergoes a structural phase transition, reorganizing into a new crystal structure.

Here we examined the phonon dynamical stability and vibrational properties based on passively trained MTPs, which had been shown to provide a stable, efficient, and convenient solution for examining phononic properties over a range of diverse compounds (Mortazavi et al. 2020).

The calculated full phonon dispersion across with respect to the high-symmetry lines in the first Brillouin zone (wave-vector) are shown in Fig. 11 and SI Fig. 7. The parental hexahydrate structure was found dynamically stable. The hypothesized structure for the tetrahydrate crystal exhibited dynamic stability as well, at least at low temperatures. The stability held regardless of the phonons being calculated on a PBE-D3 or B3LYP-D3 optimized structure. This further confirms the robustness of the approach and the flexibility of the trained MTP.

Fit of the DFT data of $\text{MgCO}_3 \cdot 4\text{H}_2\text{O}$

The structure of $\text{MgCO}_3 \cdot 4\text{H}_2\text{O}$ calculated using DFT (CIF file from DFT simulations in Supplementary Information) was fed into Findsym (Stokes and Hatch 2005) to identify possible symmetry elements and derive the appropriate space group. With a typical RMS position shift of 0.001–0.002 and a maximum position shift of 0.00351, space group P 21a was identified. The obtained unit cell parameters and space groups were then employed as a starting model to fit the observed diffractogram using the Le Bail method in the JANA2020 software (Petříček et al. 2023). The observed and fitted patterns, together with calculated residuals, are displayed in Fig. 12. The refined lattice parameters are

$a=12.4443(5)$, $b=6.4465(3)$, $c=8.1015(4)$, $\beta=112.997(3)$, $V=598.27(5)$, $\text{Chi}^2=7.06$ (CIF file after application of Findsym and LeBail fit in Supplementary Information). It can be noted that all observed peaks were fitted by the refined unit cell, which in turn did not deviate considerably from the DFT and FindSym results. Although the crystal structure was not refined in our fit, the small difference between input and refined lattice parameters supports the DFT results. It should be stressed, moreover, that the differences between the observed diffractograms and DFT-calculation may not only arise from limited capabilities of numerical approaches in crystal structure determination but also from structural disorder affecting the experimental diffraction pattern. In fact, the structural collapse of the parental hexahydrate may generate tetrahydrate crystals with a high density of stacking faults and small crystalline domains. These structural elements influenced experimental data but could not be taken into account in the DFT based structure.

Conclusions

Analyses showed that magnesium carbonate hexahydrate transformed into five different product phases. The product formation depended on the transformation conditions. Mother liquor led to a transformation into lansfordite ($T=0$ °C). Humid conditions led to basic magnesium carbonate hydrates: a dypingite-like phase at $T=20$ °C or hydromagnesite at $T=50$ °C. Dry conditions yielded an amorphous phase at $T=120$ °C or a new magnesium carbonate hydrate at $T=20$ – 50 °C. From vibrational spectroscopy it can be concluded that this new phase is a neutral magnesium carbonate hydrate. From combustion elemental analysis and thermogravimetric analysis it can be inferred that the chemical composition of the new phase is $\text{MgCO}_3 \cdot 4\text{H}_2\text{O}$.

Fig. 11 Phonon dispersion curves of magnesium carbonate hexahydrate (left) and DFT-calculated structure of magnesium carbonate tetrahydrate (right). The phonon dispersion curves were obtained by the finite differences method with MTPs passively trained over AIMD trajectories as the force constant engine. A detailed presentation of the range 0–20 THz is inserted into the Supplementary Information (SI Fig. 7)

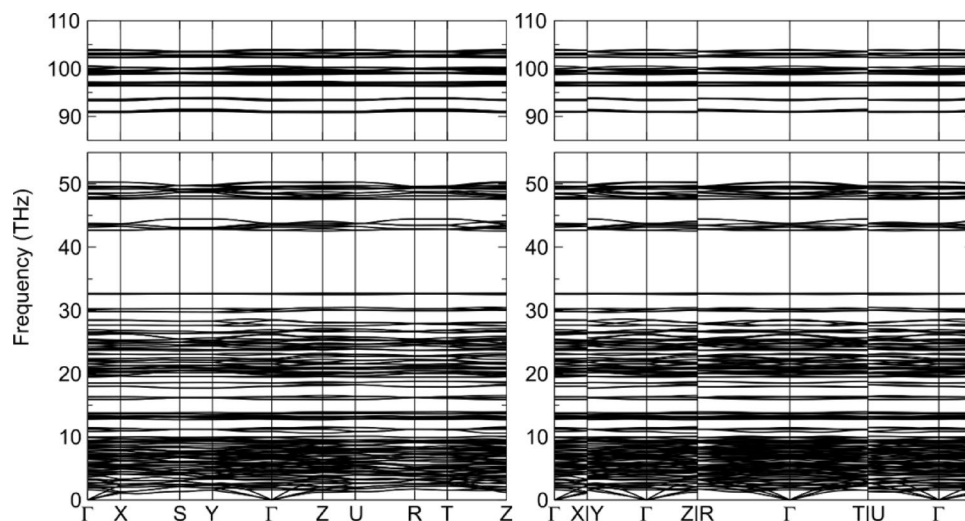
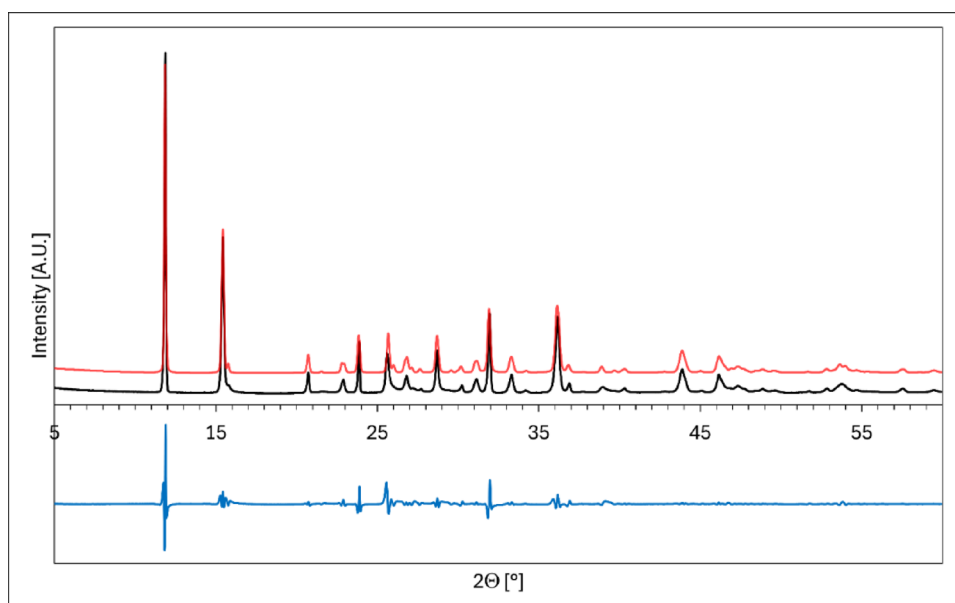


Fig. 12 X-ray powder diffractogram (CuI radiation) of the new magnesium carbonate hydrate (black). The diffractogram on top (red) shows the experimental data fitted using the Le Bail method in the JANA2020 software (Petříček et al. 2023). The difference of the two patterns is shown below (blue)



SEM imaging revealed crystal morphologies which imply a pseudomorphic transformation after the hexahydrate phase.

Therefore, it can be concluded that the transformation of magnesium carbonate hexahydrate at dry and low- T conditions proceeds via the release of weakly bonded water layers within the crystal structure. This dehydration is accompanied by a structural relaxation of the remaining magnesium carbonate tetrahydrate layers. Following this transformation route, DFT allowed the calculation of the $\text{MgCO}_3 \cdot 4\text{H}_2\text{O}$ crystal structure which was successfully validated by examining its phonon dynamical stability and vibrational properties. The transformation mechanism consisting of dehydration and structural relaxation very likely leads to a high density of stacking faults and small crystalline domains. This structural disorder is a probable cause for the persisting differences between the X-ray powder diffractogram calculated with DFT and the experimental X-ray powder diffractogram.

XPD revealed that $\text{MgCO}_3 \cdot 4\text{H}_2\text{O}$ remained being stable at room temperature when exposed to ambient air for at least 336 days. Thus, it can be concluded that, once formed in nature, $\text{MgCO}_3 \cdot 4\text{H}_2\text{O}$ may remain preserved under dry conditions for a substantial period. Its stability in aqueous solutions, however, requires further studies.

Supplementary Information The online version contains supplementary material available at <https://doi.org/10.1007/s00269-026-01349-9>.

Acknowledgements The authors wish to thank Taku Tsuchiya for editorial handling and two anonymous reviewers for their helpful comments. Furthermore, the authors thank Staatliche Naturwissenschaftliche Sammlungen Bayerns (SNSB) for kindly providing access to the Raman spectroscope, Moritz Zenkert for excellent experimental support, and Sohyun Park for fruitful discussions.

Author contributions G.J. designed the study, analyzed and interpreted the data, and drafted the manuscript. A.Z. performed the numerical characterization and drafted the numerical section of the manuscript. All authors performed experimental work, contributed to discussions, and reviewed the manuscript.

Funding Open Access funding enabled and organized by Projekt DEAL. The research did not receive funding.

Data availability No datasets were generated or analysed during the current study.

Declarations

Conflict of interest The authors declare no competing interests.

Open Access This article is licensed under a Creative Commons Attribution 4.0 International License, which permits use, sharing, adaptation, distribution and reproduction in any medium or format, as long as you give appropriate credit to the original author(s) and the source, provide a link to the Creative Commons licence, and indicate if changes were made. The images or other third party material in this article are included in the article's Creative Commons licence, unless indicated otherwise in a credit line to the material. If material is not included in the article's Creative Commons licence and your intended use is not permitted by statutory regulation or exceeds the permitted use, you will need to obtain permission directly from the copyright holder. To view a copy of this licence, visit <http://creativecommons.org/licenses/by/4.0/>.

References

- Akao M, Iwai S (1977) The hydrogen bonding of hydromagnesite. *Acta Crystallogr Sect B Struct Crystallogr Cryst Chem* 33:1273–1275
- Becke AD (1993) A new mixing of Hartree–Fock and local density-functional theories. *J Chem Phys* 98:1372–1377. <https://doi.org/10.1063/1.464304>

- Berninger UN, Jordan G, Schott J, Oelkers EH (2014) The experimental determination of hydromagnesite precipitation rates at 22.5 to 75 °C. *Mineral Mag* 78:1405–1416
- Botha A, Strydom CA (2003) DTA and FT-IR analysis of the rehydration of basic magnesium carbonate. *J Therm Anal Cal* 71:987–995
- Canterford JH, Tsambourakis G, Lambert B (1984) Some observations on the properties of dypingite, $Mg_5(CO_3)_4(OH)_2 \cdot 5H_2O$, and related minerals. *Mineral Mag* 48:437–442
- Chaka AM, Felmy AR (2014) Ab initio thermodynamic model for magnesium carbonates and hydrates. *J Phys Chem A* 118:7469–7488. <https://doi.org/10.1021/jp500271n>
- Davies PJ, Bubela B (1973) The transformation of nesquehonite into hydromagnesite. *Chem Geol* 12:289–300
- Dell RM, Weller SW (1959) The thermal decomposition of nesquehonite $MgCO_3 \cdot 3H_2O$ and magnesium ammonium carbonate $MgCO_3 \cdot (NH_4)_2CO_3 \cdot 4H_2O$. *Trans Faraday Soc* 55:2203–2220
- Desgranges L, Calvarin G, Chevrier G (1996) Interlayer interactions in $M(OH)_2$: A neutron diffraction study of $Mg(OH)_2$. *Acta Crystallogr Sect B Struct Sci* 52:82–86
- Dovesi R, Saunders VR, Roetti C, Orlando R, Zicovich-Wilson CM, Pascale F, Civalieri B, Doll K, Harrison NM, Bush IJ, D'Arco P, Llunell M, Causà M, Noël Y, Maschio L, Erba A, Rerat M, Casassa S (2017) CRYSTAL17 User's Manual. University of Torino, Torino
- Dovesi R, Erba A, Orlando R, Zicovich-Wilson CM, Civalieri B, Maschio L, Rerat M, Casassa S, Baima J, Salustro S, Kirtman B (2018) Quantum-mechanical Condensed Matter Simulations with CRYSTAL. *WIREs Comput Mol Sci* 8:1–36. <https://doi.org/10.1002/wcms.1360>
- Erba A, Desmarais JK, Casassa S, Civalieri B, Donà L, Bush IJ, Searle B, Maschio L, Edith-Daga L, Cossard A, Ribaldone C, Ascrizzi E, Marana NL, Flament J, Kirtman B (2023) CRYSTAL23: A Program for Computational Solid State Physics and Chemistry. *J Chem Theory Comput* 19:6891–6932. <https://doi.org/10.1021/acs.jctc.2c00958>
- Giester G, Lengauer CL, Rieck B (2000) The crystal structure of nesquehonite, $MgCO_3 \cdot 3H_2O$, from Lavrion, Greece. *Miner Petrol* 70:153–163
- Grimme S (2006) Semiempirical GGA-Type Density Functional Constructed with a Long-Range Dispersion Correction. *J Comput Chem* 27:1787–1799. <https://doi.org/10.1002/jcc.20495>
- Grimme S, Antony J, Ehrlich S, Krieg HA (2010) Consistent and accurate ab initio parametrization of density functional dispersion correction (DFT-D) for the 94 elements H-Pu. *J Chem Phys* 132:154104. <https://doi.org/10.1063/1.3382344>
- Grimme S, Ehrlich S, Goerigk L (2011) Effect of the damping function in dispersion corrected density functional theory. *J Comput Chem* 32:456–465. <https://doi.org/10.1002/jcc.21759>
- Grimme S, Hansen A, Brandenburg JG, Bannwarth C (2016) Dispersion-corrected mean-field electronic structure methods. *Chem Rev* 116:5105–5154. <https://doi.org/10.1021/acs.chemrev.5b00533>
- Hänchen M, Prigiobbe V, Baciocchi R, Mazzotti M (2008) Precipitation in the Mg-carbonate system—effects of temperature and CO_2 pressure. *Chem Eng Sci* 63:1012–1028
- Harrison NM (2001) First principles simulation of surfaces and interfaces. *Comput Phys Commun* 137:59–73. [https://doi.org/10.1016/S0010-4655\(01\)00171-0](https://doi.org/10.1016/S0010-4655(01)00171-0)
- Harrison AL, Mavromatis V, Oelkers EH, Bénézech P (2019) Solubility of the hydrated Mg-carbonates nesquehonite and dypingite from 5 to 35°C: implications for CO_2 storage and the relative stability of Mgcarbonates. *Chem Geol* 504:123–135
- Hinuma Y, Pizzi G, Kumagai Y, Oba F, Tanaka I (2017) Band structure diagram paths based on crystallography. *Comput Mater Sci* 128:140–184. <https://doi.org/10.1016/j.commatsci.2016.10.015>
- Hopkinson L, Rutt K, Cressey G (2008) The transformation of nesquehonite to hydromagnesite in the system CaO - MgO - H_2O - CO_2 : an experimental spectroscopic study. *J Geol* 116:387–400
- Hopkinson L, Kristova P, Rutt K, Cressey G (2012) Phase transitions in the system MgO - CO_2 - H_2O during CO_2 degassing of Mg-bearing solutions. *Geochim Cosmochim Acta* 76:1–13
- Königsberger E, Königsberger LC, Gamsjäger H (1999) Low-temperature thermodynamic model for the system Na_2 - CO_3 - $MgCO_3$ - $CaCO_3$ - H_2O . *Geochim Cosmochim Acta* 63:3105–3119
- Kresse G, Furthmüller J (1996a) Efficiency of Ab-Initio total energy calculations for metals and semiconductors using a plane-wave basis set. *Comput Mater Sci* 6:15–50. [https://doi.org/10.1016/0927-0256\(96\)00008-0](https://doi.org/10.1016/0927-0256(96)00008-0)
- Kresse G, Furthmüller J (1996b) Efficient iterative schemes for Ab Initio total-energy calculations using a plane-wave basis set. *Phys Rev B* 54:11169–11186. <https://doi.org/10.1103/PhysRevB.54.11169>
- Kresse G, Joubert D (1999) From ultrasoft pseudopotentials to the projector augmented-wave method. *Phys Rev B* 59:1758–1775. <https://doi.org/10.1103/PhysRevB.59.1758>
- Lanas J, Alvarez JI (2004) Dolomitic lime: thermal decomposition of nesquehonite. *Thermochim Acta* 421:123–132
- Langmuir D (1965) Stability of carbonates in the system MgO - CO_2 - H_2O . *J Geol* 73:730–754
- Lee C, Yang W, Parr RG (1988) Development of the Colle-Salvetti correlation-energy formula into a functional of the electron density. *Phys Rev B* 37:785–789. <https://doi.org/10.1103/PhysRevB.37.785>
- Lindner M, Saldi GD, Carrocci S, Bénézech P, Schott J, Jordan G (2018) On the growth of anhydrous Mg-bearing carbonates – Implications from norsethite growth kinetics. *Geochim Cosmochim Acta* 238:424–437
- Liu BN, Zhou XT, Cui XS, Tang JG (1990) Synthesis of lansfordite $MgCO_3 \cdot 5H_2O$ and its crystal structure investigation. *Sci China B* 33:1350–1356
- Lu Y, Sednev-Lugovets A, Carvalho P, Guzik MN, Dayaghi AM, Dunkel K, Austrheim H, Lin Z, Friis H (2025) Dypingite as a hydration series with reversible change of H_2O content. *American Mineralogist* in press. <https://doi.org/10.2138/am-2024-9603>
- Lukačević I (2011) High pressure lattice dynamics, dielectric and thermodynamic properties of SrO. *Physica B* 406:3410–3416. <https://doi.org/10.1016/j.physb.2011.06.010>
- Mavromatis V, Pearce CR, Shirokova LS, Bundeleva IA, Pokrovsky OS, Bénézech P, Oelkers EH (2012) Magnesium isotope fractionation during hydrous magnesium carbonate precipitation with and without cyanobacteria. *Geochim Cosmochim Acta* 76:161–174
- McQueen N, Vaz Gomes K, McCormick C, Blumanthal K, Pisciotta M, Wilcox J (2021) A review of direct air capture (DAC): scaling up commercial technologies and innovating for the future. *Prog Energy* 3:032001
- Ming DW, Franklin WT (1985) Synthesis and Characterization of Lansfordite and Nesquehonite. *Soil Sci Soc Am J* 49:1303–1308
- Momma K, Izumi F (2011) VESTA 3 for three-dimensional visualization of crystal, volumetric and morphology data. *J Appl Crystallogr* 44:1272–1276
- Monkhorst HJ, Pack JD (1976) Special Points for Brillouin-Zone Integrations. *Phys Rev B* 13:5188–5192. <https://doi.org/10.1103/PhysRevB.13.5188>
- Morgan B, Wilson S, Madsen IC, Gozukara YM, Habsuda J (2015) Increased thermal stability of nesquehonite ($MgCO_3 \cdot 3H_2O$) in the presence of humidity and CO_2 : implications for low-temperature CO_2 storage. *Int J Greenh Gas Control* 39:366–376
- Morgan B, Wilson S, Madsein IC, Gozukara YM, Kimpton JA, Maynard-Casley HE (2025) Magnesite formation during nesquehonite decomposition in the presence and absence of retained

- self-generated gases and the role of X-ray amorphous materials as essential stores for CO₂. *Am Miner* 110:699–708
- Mortazavi B, Novikov IS, Podryabinkin EV, Roche S, Rabczuk T, Shapeev AV, Zhuang X (2020) Exploring phononic properties of two-dimensional materials using machine learning interatomic potentials. *Appl Mater Today* 20:100685. <https://doi.org/10.1016/j.apmt.2020.100685>
- Muscat J, Wander A, Harrison NM (2001) On the prediction of band gaps from hybrid functional theory. *Chem Phys Lett* 342:397–401. [https://doi.org/10.1016/S0009-2614\(01\)00616-9](https://doi.org/10.1016/S0009-2614(01)00616-9)
- Novikov IS, Gubaev K, Podryabinkin EV, Shapeev AV (2021) The MLIP package: moment tensor potentials with MPI and active learning. *Mach Learn Sci Technol* 2:025002. <https://doi.org/10.1088/2632-2153/abc9fe>
- Oelkers EH, Gislason SR, Matter J (2008) Mineral carbonation of CO₂. *Elements* 4:333–337
- Pascale F, Zicovich-Wilson CM, López Gejo F, Civalleri B, Orlando R, Dovesi R (2004) The calculation of the vibrational frequencies of crystalline compounds and its implementation in the CRYSTAL code. *J Comput Chem* 25:888–897. <https://doi.org/10.1002/jcc.20019>
- Patel M, Mallia G, Liborio L, Harrison NM (2012) Water adsorption on rutile TiO₂(110) for applications in solar hydrogen production: a systematic hybrid-exchange density functional study. *Phys Rev B* 86:1–15. <https://doi.org/10.1103/PhysRevB.86.045302>
- Perdew JP, Burke K, Ernzerhof M (1996) Generalized gradient approximation made simple. *Phys Rev Lett* 77:3865–3868. <http://doi.org/10.1103/PhysRevLett.77.3865>
- Petříček V, Palatinus L, Plášil J, Dušek M JANA 2020 – a new version of the crystallographic computing system JANA. *Z. Kristallogr* 238: 271–282., Roetti R (2023) C (1988) Hartree-Fock Ab Initio Treatment of Crystalline Systems; Lecture Notes in Chemistry. Springer Berlin Heidelberg. <https://doi.org/10.1007/978-3-642-93385-1>
- Podryabinkin EV, Shapeev AV (2017) Active learning of linearly parametrized interatomic potentials. *Comput Mater Sci* 140:171–180. <https://doi.org/10.1016/j.commatsci.2017.08.031>
- Raade G (1970) Dypingite, a new hydrous basic carbonate of magnesium, from Norway. *Am Mineral* 55:1457–1465
- Rincke (2018) Zur Bildung von Hydrogencarbonaten mehrwertiger Metalle. Dissertation. Technische Universität Bergakademie Freiberg. <https://nbn-resolving.org/urn:nbn:de:bsz:105-qucosa-2-316291>
- Rincke C, Schmidt H, Voigt W (2020) A new hydrate of magnesium carbonate, MgCO₃·6H₂O. *Acta Cryst C* 76:244–249
- Saldi GD, Jordan G, Schott J, Oelkers EH (2009) Magnesite growth rates as a function of temperature and saturation state. *Geochim Cosmochim Acta* 73:5646–5657
- Santamaría-Pérez D, Chuliá-Jordán R, Gonzalez-Platas J, Otero-de-la-Roza A, Ruiz-Fuertes J, Pellicer-Porres J, Oliva R, Popescu C (2024) Polymorphism and phase stability of hydrated magnesium carbonate nesquehonite MgCO₃·3H₂O: negative axial compressibility and thermal expansion in a cementitious material. *Cryst Growth Des* 24(3):1159–1169
- Schott J, Dandurand JL (1975) Sur la stabilité des carbonates naturels. Valeurs Nouvelles des enthalpies libres de formation des phases des systèmes MgO-CO₂-H₂O et CaO-MgO-CO₂-H₂O. *C R Acad Sc Paris C* 280:1247–1251
- Shortt I, Gopalan V, Ura J, Singh D, Sant G, La Plante E (2024) Growth and transformation of hydrated magnesium carbonates under near-ambient conditions. *Cryst Growth Des* 24:10193–10202
- Stokes HT, Hatch DM (2005) Program for identifying the space group symmetry of a crystal. *J Appl Cryst* 38:237–238
- Suzuki J, Ito M (1973) A new magnesium carbonate hydrate mineral, Mg₅(CO₃)₄·(OH)₂·8H₂O, from Yoshikawa, Aichi prefecture, Japan. *J Japan Assoc Min Petr Econ Geol* 68:353–361
- Vilela Oliveira D, Laun J, Peintinger MF, Bredow T (2019) BSSE-correction scheme for consistent Gaussian basis sets of double- and triple-zeta valence with polarization quality for solid-state calculations. *J Comput Chem* 40:2364–2376. <https://doi.org/10.1002/jcc.26013>
- White WB (1971) Infrared characterization of water and hydroxyl ion in the basic magnesium carbonate minerals. *Am Mineral* 56:46–53
- Yang P, Bracco JN, Camacho Meneses G, Yuan K, Stubbs JE, Boamah MD, Brahlek M, Sassi M, Eng PJ, Boebinger MG, Borisevich A, Wanhala AK, Wang Z, Rosso KM, Stack AG, Weber J (2025) Carbonation of MgO single crystals: implications for direct air capture of CO₂. *Environ Sci Technol* 59:3484–3494
- Zicovich-Wilson CM, Pascale F, Roetti C, Saunders VR, Orlando R, Dovesi R (2004) Calculation of the vibration frequencies of α-quartz: the effect of Hamiltonian and basis set. *J Comput Chem* 25:1873–1881. <https://doi.org/10.1002/jcc.20120>
- Zunger A (2019) Beware of plausible predictions of fantasy materials. *Nature* 566:447–449. <https://doi.org/10.1038/d41586-019-00676-y>

Publisher's Note Springer Nature remains neutral with regard to jurisdictional claims in published maps and institutional affiliations.